C. Ciulla et al. (2017) Int. J. Appl. Sci. Biotechnol. Vol 5(3): 326-335
DOI: 10.3126/ijasbt.v5i3.18271

ISSN (Online): 2091-2609
DOI Prefix: 10.3126/ijasbt

International Journal of Applied Sciences and Biotechnology (IJASBT)

Research Article

The Intensity-Curvature of Human Brain Vessels Detected with Magnetic Resonance Imaging

Carlo Ciulla[1*], Ustijana Rechkoska Shikoska[1], Dimitar Veljanovski[2], Filip A. Risteski[2]

[1]University of Information Science & Technology, "St. Paul the Apostle", Partizanska B.B., Ohrid, 6000, Republic of Macedonia
[2]Department of Radiology, General Hospital 8-mi Septemvri, Boulevard 8th September, Skopje, 1000, Republic of Macedonia

Abstract

The intensity-curvature term is the concept at the root foundation of this paper. The concept entails the multiplication between the value of the image pixel intensity and the value of the classic-curvature (CC(x, y)). The CC(x, y) is the sum of all of the second order partial derivatives of the model polynomial function fitted to the image pixel. The intensity-curvature term (ICT) before interpolation $E_0(x, y)$ is defined as the antiderivative of the product between the pixel intensity and the classic-curvature calculated at the origin of the pixel coordinate system (CC(0, 0)). The intensity-curvature term (ICT) after interpolation $E_{IN}(x, y)$ is defined as the antiderivative of the product between the signal re-sampled by the model polynomial function at the intra-pixel location (x, y) and the classic-curvature. The intensity-curvature functional (ICF) is defined as the ratio between $E_0(x, y)$ and $E_{IN}(x, y)$. When the ICF is almost equal to the numerical value of one ('1'), $E_0(x, y)$ and $E_{IN}(x, y)$ are two additional domains (images) where to study the image from which they are calculated. The ICTs presented in this paper are able to highlight the human brain vessels detected with Magnetic Resonance Imaging (MRI), through a signal processing technique called inverse Fourier transformation procedure. The real and imaginary parts of the k-space of the ICT are subtracted from the real and imaginary parts of the k-space of the MRI signal. The resulting k-space is inverse Fourier transformed, and the human brain vessels are highlighted.

Keywords: Magnetic resonance imaging; inverse Fourier transformation procedure; intensity-curvature term; k-space.

Introduction

The Literature

Taking advantage of the magnetic susceptibility of deoxyhemoglobin, at ultra-high field (UHF) MRI offers the possibility to image the vasculature of the human brain (Christoforidis *et al*., 1999). The localization and the identification of the human brain vasculature is therefore tight to changes in the susceptibility of the human brain tissues. The MRI technique called Susceptibility Weighted Imaging (SWI) which is based on gradient echo scans (T2* imaging) combined with unwrapped high-pass filtered phase images, provides the MRI images with contrast enhancement sufficient to image the vasculature, to enhance

Article may be cited as:

C. Ciulla *et al*. (2017) Int. J. Appl. Sci. Biotechnol. Vol 5(3): 326-335. DOI: http://dx.doi.org/10.3126/ijasbt.v5i3.18271

***Corresponding author**
Carlo Ciulla,
University of Information Science & Technology, "St. Paul the Apostle", Partizanska B.B., Ohrid, 6000, Republic of Macedonia
Email: carlo.ciulla@uist.edu.mk, cxc2728@njit.edu

white/gray matter contrast, to enhance water/fat contrast, to identify iron (Haacke *et al*., 2007) and other brain structures that are not background tissue (Haacke *et al*., 2004; Liu *et al*., 2015). Through the image processing technique called Maximum Intensity Projection (MIP), SWI is able to visualize vessel connectivity (Haacke *et al*., 2009), also venous structures and hemorrhages (Mittal *et al*., 2009). Imaging the human brain vasculature is very important when diagnosing stroke patients (Chen *et al*., 2010), and in such cases the diagnostic protocol comprises of the following techniques: (i) contrast-enhanced MRI, (ii) MR angiography, (iii) cerebral angiography, (iv) transcranial Doppler, and (v) Single Photon Emission Computed Tomography (SPECT) (Christoforidis *et al*., 1999). Fluid Attenuated Inversion Recovery (FLAIR) MRI is a viable technique for the identification of hyper-intense vessels which might trigger stroke in the human brain (Kamran *et al*., 2000). In recent years, the use of SWI has been extended to MR venography using the shift in resonance frequency between the venous vessel and the surrounding tissue. The resonance shift is caused by paramagnetic deoxyhemoglobin located in veins (Koopmans *et al*., 2008). Nowadays, MR venography can image small vessels of the human brain, through the use of deoxyhemoglobin as diffusible tracer (Reichenbach *et al*., 1997). Arterial Spin Labeling (ASL) MRI is used to label the blood water in the human brain vessels (Detre *et al*., 2012). Regional ASL MRI offers the advantage to measure the perfusion of the anterior and posterior circulation separately (Günther *et al*., 2006). MR angiography at ultra-high magnetic fields can image non-invasively the microvasculature of the brain (Cho *et al*., 2008).

Because of the technological efforts of the recent years, Magnetic Resonance Angiography (MRA) and contrast enhanced MRA, are among the most promising MR techniques that can be used to image the human brain vasculature (Preim and Oeltze, 2008; Sakuma, 2011). The MRA signal is detected because of the difference in radiofrequency excitation existing between stationary saturated venous blood protons and incoming non saturated blood protons (Miyazaki and Lee, 2008). Post-processing is necessary in order to make MRA available to clinical routine and it comprises of cerebrovascular segmentation and vessels delineation. The combination of the Gaussian kernel used for filtering and the Hessian of the Gaussian image as the derivative operator is the basis of the vesselness technique, which is used to improve vessel delineation (Sato *et al*., 1998; Frangi *et al*., (1998); Frangi, 2001). Moreover, recent research reports cerebrovascular segmentation through the fusion of intensity and vesselness using fuzzy rules (Forkert *et al*., 2011). To assess the coronary anatomy is necessary in order to diagnose several diseases and is nowadays possible through the use of both Computed Tomography (CT) and MR Angiography (Post *et al*., 1996). A recent study concerned with the diagnosis of coronary artery disease (CAD), compares conventional coronary anatomy performed with CT and Magnetic Resonance Imaging (MRI) as opposed to conventional coronary angiography (CAG), and finds CT more accurate than MRI (Schuetz *et al*., 2010).

The Motivation of the Study

The intensity-curvature term is defined as the product between the image pixel intensity and the sum of all of the second order partial derivatives (with respect to the dimensional variables) of the model function fitted to the image pixel. Such sum is called classic-curvature (Ciulla *et al*., 2015). The motivation of the present study originates from the evidence that some polynomial model functions have the property by which there exists striking similarity between the intensity-curvature terms (ICTs) before interpolation and after interpolation (Ciulla *et al*., 2017). This similarity makes the ratio between ICTs (which is called intensity-curvature functional (ICF)) very close to the numerical value of one ('1') across the all spatial extent of the image, and therefore makes the ICF useless. In such cases, despite the loss of information due to an unusable ICF, the ICTs ($E_0(x, y)$ and $E_{IN}(x, y)$) can still be utilized (Ciulla *et al*., 2017). This paper presents the study of the behaviour of the ICTs calculated from two polynomial model functions called B32D and G42D (Ciulla *et al*., 2017). The study is carried out through a novel approach, which makes it possible to delineate human brain Magnetic Resonance Imaging (MRI) detected vasculature. The approach is based on the inverse Fourier transformation of the difference between the k-space of the MRI and the k-space of the intensity-curvature term (ICT). The difference comprises of: (i) the real part of the k-space of the MRI minus the real part of the k-space of the intensity-curvature term; and (ii) the imaginary part of the k-space of the MRI minus the imaginary part of the k-space of the intensity-curvature term. After the difference is calculated, the real and imaginary parts are inverse Fourier transformed, and thus the reconstructed signal is obtained.

Materials and Methods

Magnetic Resonance Imaging of one healthy subject was recorded with the pulse sequences parameters indicated in Table 1, where: TE is the Time to Echo; TR is the repetition time; FOV is the field of view. The magnet was the Magnetom Essenza, Siemens with strength 1.5 T. The measurement protocol was the localizer. The MRI scanning procedures were conducted in compliance with the ethical standards set by the General Hospital 8-mi Septemvri, Skopje – Republic of Macedonia, which is the institution where the subject was studied. Informed consent was properly administered prior to the MRI scanning procedure. The mathematics of the two model polynomial functions (B32D and G42D) utilized in this research and the math procedures necessary to calculate the intensity-curvature terms are reported elsewhere (Ciulla *et al*., 2017). This

paper reports on the applications the ICTs and the use of the ICTs by means of the inverse Fourier transformation procedure.

Table 1: The recording parameters of the MRI images.

MRI acquisition	Fig. 1	Figs. 2, 3, 4, 5
TE	96 msec	2.59 msec
TR	5050 msec	7 msec
FOV	204 x 250	280 x 280
Pixel matrix size	196 x 320	410 x 512
# of slices	28	18

Results

The Intensity-Curvature Functional

The intensity-curvature functional (ICF) of the bivariate cubic polynomial model termed B32D, and the ICF of the bivariate cubic Lagrange polynomial model termed G42D, is a ratio which value is near the numerical value of one ('1') overall the full spatial extent of the image.

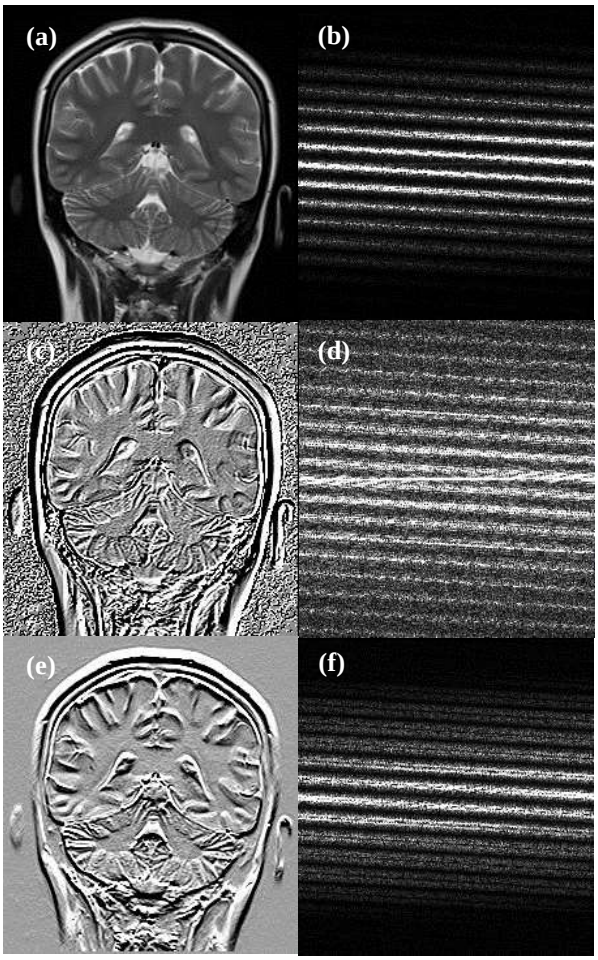

Fig. 1: MRI in (a). (b) K-space of (a). (c) The intensity-curvature functional of (a). (d) K-space of (c). (e) The high pass filtered MRI. (f) K-space of (e). The bivariate linear function was fitted to the MRI data because its ICF is an image which pixel intensity values are not equal to one ('1').

This happens when the option provided by the program in order to process the signal is: 'n' (normalize). Note that the aforementioned behaviour of the ICF is not common to other mathematical functions, such as for instance the bivariate linear model function. It is due to acknowledge that the ICF is similar to MRI high pass filtered signal and as such it is useful as an alternative high pass filter of the MRI signal (Ciulla *et al*., 2016). It is also due to report, as Fig. 1 shows, that the k-space of the MRI high pass filtered signal is different from the k-space of the ICF (Ciulla *et al*., 2017). Thus, the ICF and the MRI high pass filtered signal are not the same (Ciulla *et al*., 2017). The next section of the paper presents the study of the human brain vasculature with the ICTs.

The Study of the Intensity-Curvature Terms with Applications to MRI Human Brain Vasculature

The MRI images were cropped and divided in two classes: control zones (5) and regions of interest (ROIs) (20). For each control zone and for each region of interest, the ICTs were calculated when the equations of two polynomial model functions were fitted to the MRI data. Thus, for a selected control zone or region of interest, four ICTs were calculated. Fig. 2 shows four cases.

Each case comprises of ten pictures: one MRI image, four ICTs images and five k-space images. Each case is labelled with letters: (a) through (j); and with letters and numbers (to distinguish among cases located in the same figure: for instance (a.1) through (j.1)). Figs. 2 and 3 show: (i) the MRI zone studied (a); (ii) the $E_0(x, y)$ and the $E_{IN}(x, y)$ calculated from the bivariate cubic polynomial model (B32D) (see (b) and (d) respectively); (iii) the $E_0(x, y)$ and the $E_{IN}(x, y)$ calculated from the bivariate cubic Lagrange polynomial model (G42D) (see (c) and (e) respectively). Figs. 2 and 3, show in (f), (g), (h), (i) and (j) the k-space of each of (a), (b), (c), (d) and (e) respectively. Careful selection of the control zones and regions of interest is assured because the choice of the control zones display only cortical surface, whereas the regions of interest where chosen so to make sure that the image was inclusive of vasculature structures also. In Figs. 2 and 3, both $E_0(x, y)$ and $E_{IN}(x, y)$ were calculated using the bivariate cubic polynomial model (B32D) and they have filtering effect on the MRI. It is visible in the pictures that the cortical surface is flattened and the vasculature is highlighted. Such behaviour finds confirmation in the k-space of the images. Specifically, the k-space of the MRI (a) (which is presented in (f.x)) shows additional frequencies versus the k-space in (g.x) and (i.x). Thus, in (b.x) and (d.x), the vasculature structures are isolated on a flattened cortical surface and the vasculature is well distinct (see Figs. 2 and 3). This occurrence suggests that the ICTs calculated from B32D do filter the MRI. This effect is also visible when the analysis is focused on the control zones (see Figs. 2 and 3). Note that 'x' is the image

label identifier. For instance, in Fig. 2, (a.x) means: (a.1), (a.2) and (a.3). Likewise, in Fig. 3, (a.x) means: (a.1) and (a.2). The intensity-curvature terms (ICTs) of the bivariate cubic Lagrange polynomial (G42D) display an effect similar to the ICTs calculated from the bivariate cubic polynomial model (B32D). Such effect suggests that the ICTs calculated from the polynomial model termed G42D do filter the MRI also. To see the aforementioned effect, look at the k-space in (g.x) and (i.x) in Figs. 2 and 3, and compare the k-space images to the k-space image calculated from the MRI, which is displayed in (f.x). Some frequency components are missing in (g.x) and (i.x). Although, visible in the ICTs images calculated from the bivariate cubic Lagrange polynomial model (G42D), the filtering effect is more accentuated in the ICTs calculated from the bivariate cubic polynomial model (B32D) (see (b.x) and (d.x) of Figs. 2 and 3). Overall, the results show that the ICTs have imaging capabilities that make them suitable to highlight (delineate) the human brain vasculature imaged with MRI. In Fig. 4, the difference between the k-space of the MRI and ICT is calculated by the subtraction of the real and imaginary parts of the k-space. Which is, the real part of the k-space of the MRI, minus, the real part of the k-space of the intensity-curvature term. And, the imaginary part of the k-space of the MRI, minus, the imaginary part of the k-space of the intensity-curvature term. After the difference is calculated, the real and imaginary parts obtained through it, are inverse Fourier transformed, and thus the reconstructed signal is obtained. (a.3), (a.5), (a.7), (a.8), (a.9) Are control zones.

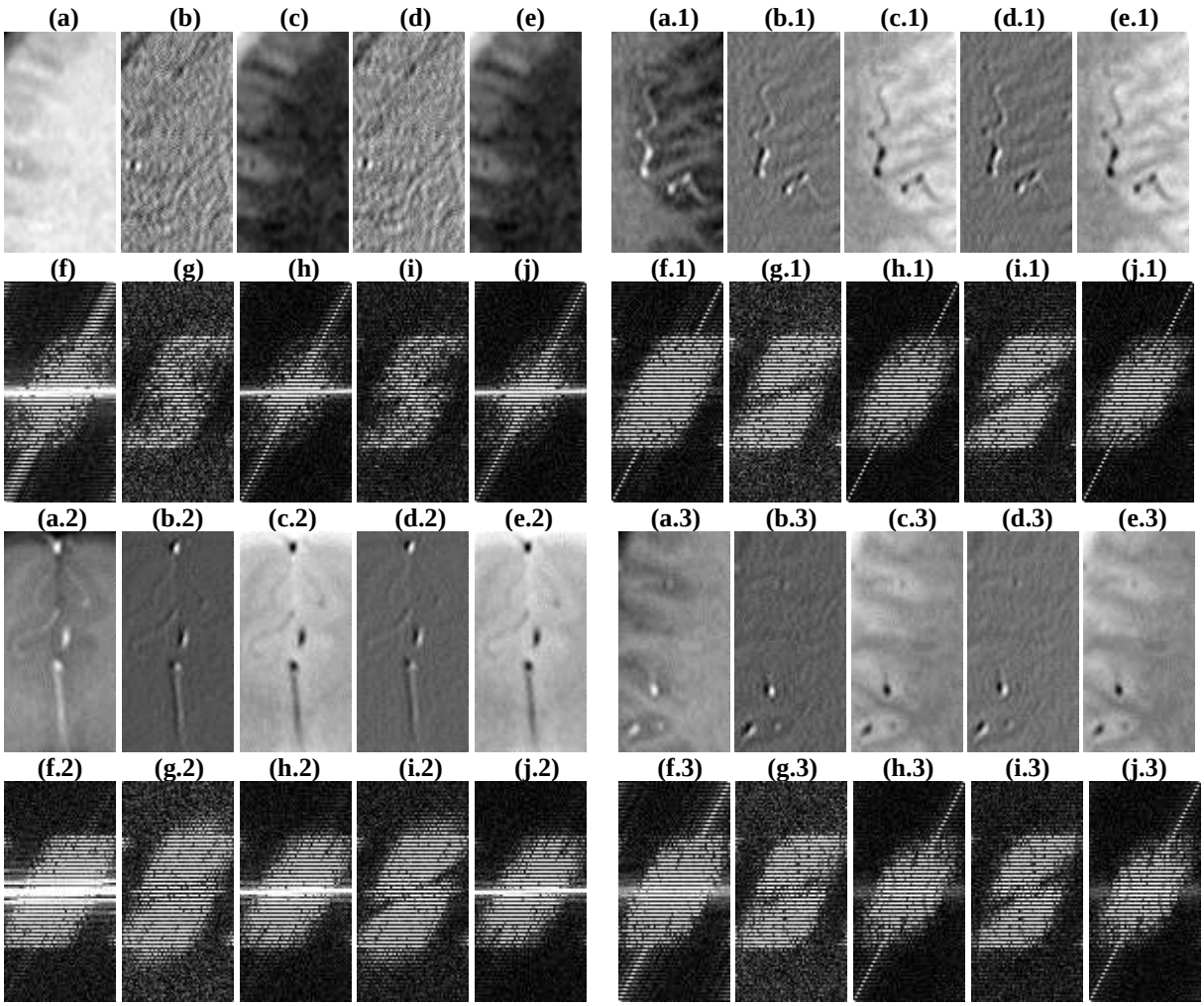

Fig. 2: Control zone selected in the human brain MRI: (a). The intensity-curvature terms before interpolation: calculated from B32D and presented in (b), calculated from G42D and presented in (c). The intensity-curvature terms after interpolation: calculated from B32D and presented in (d), calculated from G42D and presented in (e). (f) The k-space of (a). (g) and (h) The k-space of (b) and (c). (i) and (j) The k-space of (d) and (e). Vasculature in the human brain MRI: (a.1), (a.2), (a.3). The intensity-curvature terms before interpolation: calculated from B32D and presented in (b.1), (b.2) and (b.3); calculated from G42D and presented in (c.1), (c.2) and (c.3). The intensity-curvature terms after interpolation: calculated from B32D and presented in (d.1), (d.2) and (d.3); calculated from G42D and presented in (e.1), (e.2) and (e.3). (f.1), (f.2), (f.3) The k-space of (a.1), (a.2), (a.3), respectively. The k-space of (b.1), (b.2), (b.3) and (c.1), (c.2), (c.3) is in (g.1), (g.2), (g.3) and (h.1), (h.2), (h.3), respectively. The k-space of (d.1), (d.2), (d.3) and (e.1), (e.2), (e.3) is in (i.1), (i.2), (i.3) and (j.1), (j.2), (j.3), respectively. All images have pixel matrix size 57x113.

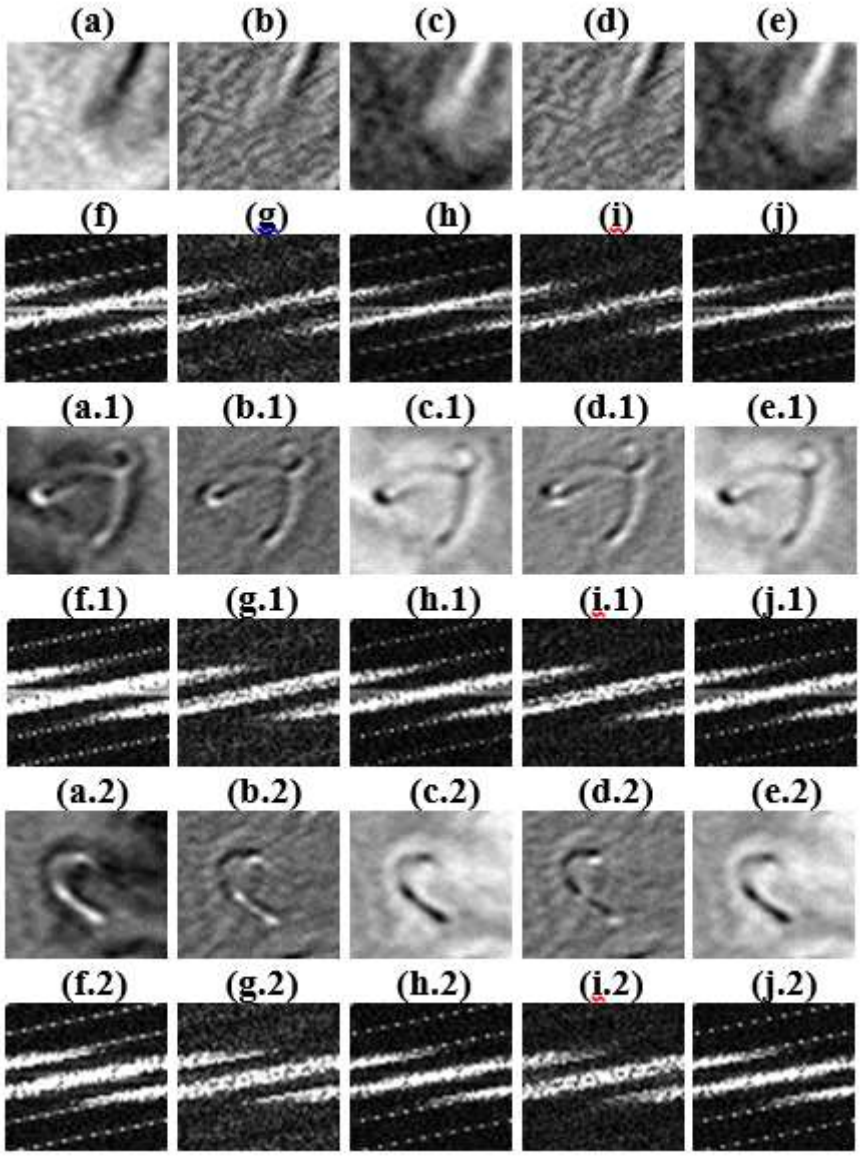

Fig. 3: Control zone selected in the human brain MRI: (a). The intensity-curvature terms before interpolation: calculated from B32D and presented in (b); calculated from G42D and presented in (c). The intensity-curvature terms after interpolation: calculated from B32D and presented in (d); calculated from G42D and presented in (e). (f) The k-space of (a). (g) and (h) The k-space of (b) and (c). (i) and (j) The k-space of (d) and (e). Vasculature in the human brain MRI: (a.1), (a.2). The intensity-curvature terms before interpolation: calculated from B32D and presented in (b.1) and (b.2); calculated from G42D and presented in (c.1) and (c.2). The intensity-curvature terms after interpolation: calculated from B32D and presented in (d.1) and (d.2); calculated from G42D and presented in (e.1) and (e.2). (f.1), (f.2) The k-space of (a.1), (a.2), respectively. (g.1), (g.2) and (h.1), (h.2) The k-space of (b.1), (b.2) and (c.1), (c.2), respectively. (i.1), (i.2) and (j.1), (j.2) The k-space of (d.1), (d.2) and (e.1), (e.2), respectively. All images have pixel matrix size of 56x51.

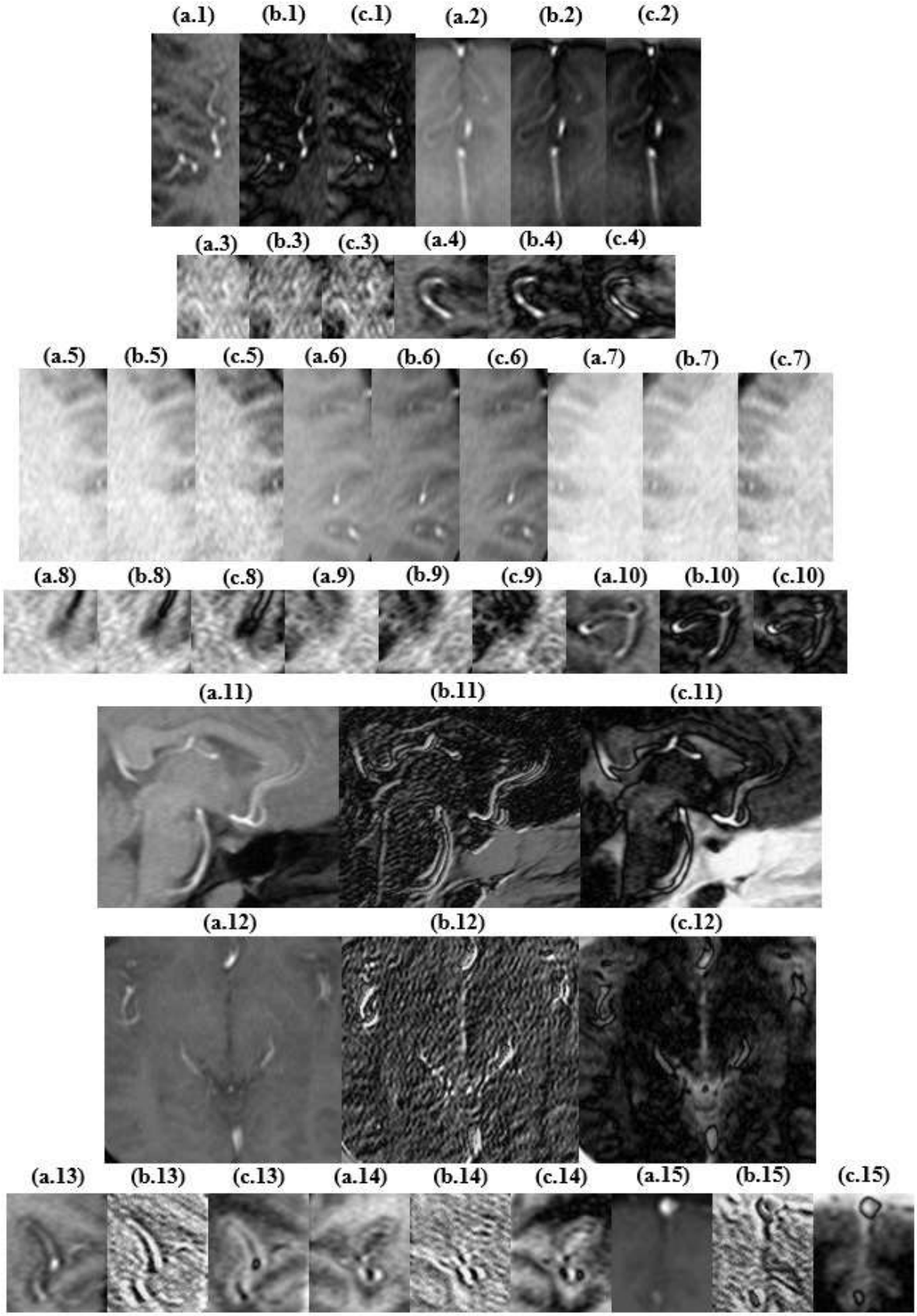

Fig. 4: MRI images in: (a.1), (a.2), (a.3), (a.4), (a.5), (a.6), (a.7), (a.8), (a.9), (a.10), (a.11), (a.12), (a.13), (a.14), and (a.15). The reconstructed signal after inverse Fourier transformation of the difference between the k-space of the MRI and the k-space of the intensity-curvature term (calculated from the polynomial model function termed B32D) is presented in (b.1), (b.2), (b.3), (b.4), (b.5), (b.6), (b.7), (b.8), (b.9), (b.10), (b.11), (b.12), (b.13), (b.14) and (b.15). The signal reconstructed after inverse Fourier transformation of the difference between the k-space of the MRI and the k-space of the intensity-curvature term (calculated from the polynomial model function termed G42D) is presented in (c.1), (c.2), (c.3), (c.4), (c.5), (c.6), (c.7), (c.8), (c.9), (c.10), (c.11), (c.12), (c.13), (c.14), (c.15).

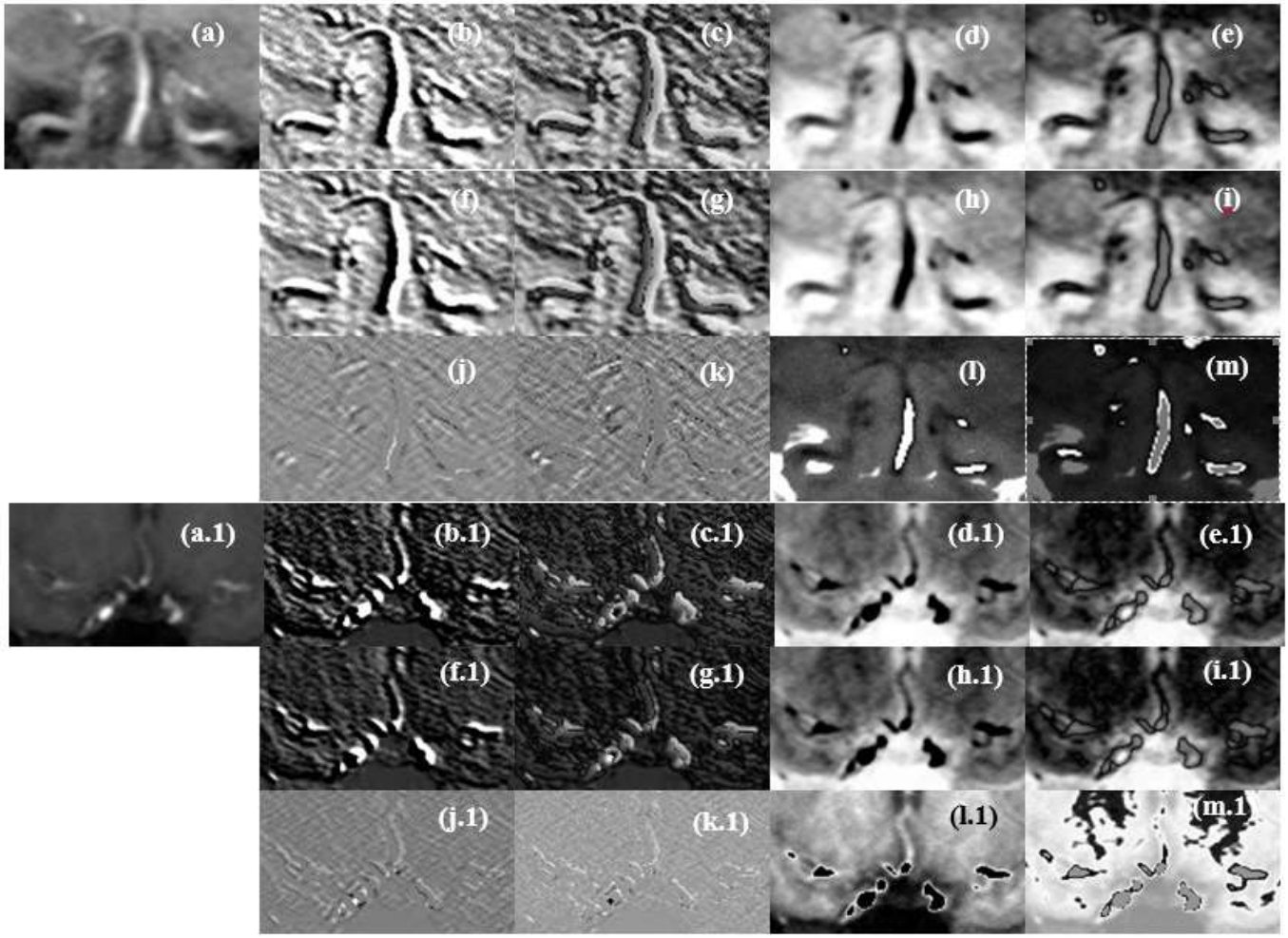

Fig. 5: MRI images: (a), (a.1). The ICT before interpolation (E_0 (x, y)) calculated from the polynomial model function termed B32D is presented in (b) and (b.1), and the reconstructed signal is presented in (c) and (c.1). The ICT before interpolation (E_0 (x, y)) calculated from the polynomial model function termed G42D is presented in (d) and (d.1), and the reconstructed signal is presented in (e) and (e.1). The ICT after interpolation (E_{IN} (x, y)) calculated from the polynomial model function termed B32D is presented in (f) and (f.1), and the reconstructed signal is presented in (g) and (g.1). The ICT after interpolation (E_{IN} (x, y)) calculated from the polynomial model function termed G42D is presented in (h) and (h.1), and the reconstructed signal is presented in (i) and (i.1), respectively. Difference images: (b) minus (f) is in (j); (b.1) minus (f.1) is in (j.1); (c) minus (g) is in (k); (c.1) minus (g.1) is in (k.1); (d) minus (h) is in (l); (d.1) minus (h.1) is in (l.1); (e) minus (i) is in (m); (e.1) minus (i.1) is in (m.1). The images (a) through (m) have pixel matrix size 118x77. The images (a.1) through (m.1) have pixel matrix size 152x85 and to the purpose of the presentation in the figure, they were resized maintaining the aspect ratio.

The results presented in Fig. 4 show highlight of the vessels, which is featured mostly by the suppression of the tissue and the enhancement of the vessels visibility (the ICTs were all 'before interpolation': (E_0)). Thus, in essence, the procedure has the effect of filtering out the MRI images. Table 2 reports the pixel matrix size of the MRI images and the ICTs images presented in Fig. 4. The research presented in this paper contributes two additional domains where is possible to observe and study the human brain vasculature: the ICTs. However, the main contribution of the study is to delineate the vasculature of the human brain through the use of the ICTs in the inverse Fourier transformation procedure. The filtering effect is visible through the analysis of the k-space presented in Figs. 2 and 3. The ICTs calculated from the bivariate cubic polynomial model (B32D) make the filtering effect on the MRI more accentuated than the filtering effect obtained when fitting the bivariate cubic Lagrange polynomial model (G42D).

Table 2: Regions of interest (ROI(s)) and pixel matrix size of the MRI images.

ROI(s)	**1/5/6**	**2/7**	**3**
Pixel matrix size	53x116	57x113	43x50
ROI(s)	**4/8/9/10**	**11**	**12**
Pixel matrix size	56x51	183x154	181x175

In the top row and the third row from the top are reported the label of the triplet of images identifiable in Fig. 4 with: (a.x), (b.x), (c.x). For instance, the MRI image label '1' identifies the images (a.1), (b.1) and (c.1) (see Fig. 4), and the ROI is the MRI presented in (a.1). In the second row and the bottom row are reported the corresponding pixel matrix size of the images.

The filtering effect is also visible in the ICTs images where the vasculature is highlighted and the rest of the brain cortex is moderately flattened (see (b.x) and (d.x) in Figs. 2 and 3).

The filtering effect of the ICTs is also visible in Figs. 4 and 5. In Figs. 4 and 5, the k-space of the ICT is subtracted from the k-space of the MRI, the resulting k-space is inverse Fourier transformed, and the outcome is again to highlighting the human brain vessels.

Discussion

When studying the properties of SWI imaging, is possible to characterize the magnetic susceptibility versus the vessel size, to create novel venograms on the basis of susceptibility maps (Haacke *et al*., 2010; 2015), and to map the $T2^*$ relaxation time (Denk and Rauscher, 2010). A growing number of research groups have developed techniques providing quantitative measures of magnetic susceptibility (Liu *et al*., 2015; Wang and Liu, 2015). The use of MRI techniques like MR Angiogram (MRA), and MR Venogram (MRV) at ultra-high field show increased susceptibility (Von Morze *et al*., 2007; Bae *et al*., 2010) versus 3T, and increased capability to distinguish between arteries and veins (Duvernoy *et al*., 1981). The increased susceptibility obtained with SWI at 7T makes it possible to see changes in image contrast and is a consequence of low oxygenated venous blood (Deistung *et al*., 2008). MRI post-processing provides the detection of veins with diameter smaller than a pixel (Reichenbach *et al*., 1997). The importance of the determination of the vessel size has been addressed and studied within the context of tumor MRI and the feasibility to distinguish the vascular size in normal tissue and tumor had been reported (Hsu *et al*., 2009). Following contrast agent administration, which yields to change of contrast in MRI images between tissue and vasculature of the human brain, MRI techniques using the susceptibility change have been able to determine quantification of vessel dimensions. More specifically, the ratio between the changes in transverse relaxation rate constants of the spin echo R_2 and of the free induction decay R^*_2 (prior and after the injection of the contrast agent), embeds a portion of susceptibility difference between vessels and brain tissue (Tropres *et al*., 2001) and allows the quantitation of the vessels size. Similarly, Vessel Size Imaging (VSI) (Kiselev *et al*., 2005) is an MRI technique which bases the quantitative assessment of the vessel caliber on the relation between: (i) contrast-enhanced relaxation rate R^*_2 of the free induction decay, and (ii) the relaxation rate R_2 of the Spin Echo (SE). The combination of the two pulse sequences: Gradient Echo and Spin Echo, along with the injection of the contrast agent had been used in animal studies in order to quantify estimates of micro-vessel density (Jensen *et al*., 2006). For a review of traditional filtering techniques, which is inclusive of performance comparison of the detection of tubular structures, the reader is referred to work reported elsewhere (Xiao *et al*., 2013). The literature reports the use of: (i) the Gaussian and/or the Rectangular filtering kernel and (ii) the derivative operator (the Laplacian and/or the Hessian) in order to detect tubular structures and also human vessels from clinical images (Xiao *et al*., 2013). The contribution of this piece of research is the use of the intensity-curvature terms with the inverse Fourier transformation procedure. This signal processing technique is novel and is capable to delineate and highlight human brain vasculature detected with MRI.

Conclusion

The use of the intensity-curvature concept is what makes possible to delineate the human brain vasculature in MRI. The concept entails merging the image pixel intensity with the sum of second order partial derivatives of the model function fitted to the image pixel. From the concept descends the image processing techniques called intensity-curvature terms (ICTs). The motivation of the study emanates from the fact that for some model polynomial functions the intensity-curvature functional is close to the numerical value of one ('1') across the full spatial extent of the image. In the specifics, for the model polynomial functions B32D and G42D, this happens when the option provided by the program in order to process the signal is: 'n' (normalize). In such cases the study of the ICTs is consequential. The ICTs are used in this research within the context of the inverse Fourier transformation procedure. The k-space of the ICT (real and imaginary parts) is subtracted from the k-space of the human brain MRI (real and imaginary parts). The resulting k-space is inverse Fourier transformed and the resulting reconstructed signal show clear delineation of the vasculature. The results reported in this paper indicates that the highlight of the vasculature through the inverse Fourier transformation is of relevance to diagnostic biomedical imaging.

References

Bae KT, Park SH, Moon CH, Kim JH, Kaya D and Zhao T (2010) Dual-echo arteriovenography imaging with 7T MRI. *J Magn Reson Imaging* **31**:255-261. DOI: 10.1504/IJMIC.2010.032808

Chen F, Marchal G and Ni Y (2010) Rodent models and magnetic resonance imaging: diagnostic and therapeutic utilities for stroke. *Int. J. of Modelling, Identification and Control* **9**: 275-287. DOI: 10.1504/IJMIC.2010.032808

Christoforidis GA, Bourekas EC, Baujan M, Abduljalil AM, Kangarlu A, Spigos DG, Chakeres DW and Robitaille PML (1999) High resolution MRI of the deep brain vascular anatomy at 8 Tesla: susceptibility-based enhancement of the venous structures. *J Comput Assist Tomogr* **23**:857-866. DOI: http://journals.lww.com/jcat/Fulltext/1999/11000/High_Resolution_MRI_of_the_Deep_Brain_Vascular.8.aspx

Cho ZH, Kang CK, Han JY, Kim SH, Kim KN, Hong SM, Park CW and Kim YB (2008) Observation of the lenticulostriate arteries in the human brain in vivo using 7.0 T MR angiography. *Stroke* **39**:1604-1606. DOI: 10.1161/STROKEAHA.107.508002

Ciulla C, Risteski FA, Veljanovski D, Rechkoska US, Adomako E and Yahaya F (2015) A compilation on the contribution of the classic-curvature and the intensity-curvature functional to the study of healthy and pathological MRI

of the human brain. *Int. J. Applied Pattern Recognition* **2**:213-234. DOI: 10.1504/IJAPR.2015.073852

Ciulla C, Veljanovski D, Rechkoska SU and Risteski FA (2016) On the properties of the intensity-curvature measurement approaches: the classic-curvature and the intensity-curvature functional. *J Solid Tumors* **6**:33-53. DOI: http://dx.doi.org/10.5430/jst.v6n1p38

Ciulla C, Rechkoska SU, Reckoski V, Veljanovski D and Risteski FA (2017) The study of the intensity-curvature term: Applications in magnetic resonance imaging of the human brain. *Thammasat International Journal of Science and Technology* **22**:27-44.

Denk C and Rauscher A (2010) Susceptibility weighted imaging with multiple echoes. *J Magn Reson Imaging* **31**:185-191. DOI: 10.1002/jmri.21995

Deistung A, Rauscher A, Sedlacik J, Stadler J, Witoszynskyj S and Reichenbach JR (2008) Susceptibility weighted imaging at ultra-high magnetic field strengths: theoretical considerations and experimental results. *Magn Reson Med* **60**:1155-1168. DOI: 10.1002/mrm.21754

Detre JA, Rao H, Wang DJ, Chen YF and Wang Z (2012) Applications of arterial spin labeled MRI in the brain. *J Magn Reson Imaging* **35**:1026-1037. DOI: 10.1002/jmri.23581

Duvernoy HM, Delon S and Vannson JL (1981) Cortical blood vessels of the human brain brain. *Brain Res. Bull* **7**:519-579. DOI: 10.1016/0361-9230(81)90007-1

Forkert ND, Schmidt-Richberg A, Fiehler J, Illies T, Möller D, Handels H and Säring D (2011) Fuzzy-based vascular structure enhancement in time-of-flight MRA images for improved segmentation. *Methods Inf Med* **50**:74-83. DOI: 10.3414/ME10-02-0003

Frangi AF, Niessen WJ, Vincken KL, Viergever MA (1998) Multiscale vessel enhancement filtering. In: International Conference on Medical Image Computing and Computer-Assisted Intervention; Wells, W.M., Colchester, A., Delp, S.L., Eds., Lecture Notes in Computer Science, Springer Verlag: Berlin, Germany, **1496**:130-137. DOI: 10.1007/BFb0056195

Frangi AF (2001) Three-dimensional model-based analysis of vascular and cardiac images. Doctoral dissertation. University Medical Center Utrecht, The Netherlands.

Haacke EM, Xu Y, Cheng, YCN and Reichenbach JR (2004) Susceptibility weighted imaging (SWI). *Magn Reson Med* **52**:612-618. DOI: 10.1002/mrm.20198

Haacke EM, Muhammad A, Khan A, Manova ES, Krishnamurthy B, Gollapalli L, Ciulla C, Kim I, Petersen F and Kirsch W (2007) Establishing a baseline phase behavior in magnetic resonance imaging to determine normal vs. abnormal iron content in the brain. *J Magn Reson Imaging* **26**:256-264. DOI: 10.1002/jmri.22987

Haacke EM, Mittal S, Wu Z, Neelavalli J and Cheng YCN (2009) Susceptibility-weighted imaging: Technical aspects and clinical applications, part 1. *AJNR Am J Neuroradiol* **30**:19-30. DOI: 10.3174/ajnr. A1400

Haacke EM, Tang J, Neelavalli J and Cheng YCN (2010) Susceptibility mapping as a means to visualize veins and quantify oxygen saturation. *J Magn Reson Imaging* **32**:663-676. DOI: 10.1002/jmri.22276

Haacke EM, Liu S, Buch S, Zheng W, Wu D and Ye Y (2015) Quantitative susceptibility mapping: current status and future directions. *Magn Reson Imaging* **33**:1-25. DOI: 10.1016/j.mri.2014.09.004

Hsu YY, Yang WS, Lim KE and Liu HL (2009) Vessel size imaging using dual contrast agent injections. *J Magn Reson Imaging* **30**:1078-1084. DOI: 10.1002/jmri.21960

Kamran S, Bates V, Bakshi R, Wright P, Kinkel W and Miletich R (2000) Significance of hyperintense vessels on FLAIR MRI in acute stroke. *Neurology* **55**:265-269. DOI: http://dx.doi.org/10.1212/WNL.55.2.265

Kiselev VG, Strecker R, Ziyeh S, Speck O and Hennig J (2005) Vessel size imaging in humans. *Magn Reson Med* **53**:553-563. DOI: 10.1002/mrm.20383

Koopmans PJ, Manniesing R, Niessen WJ, Viergever MA and Barth M (2008) MR venography of the human brain using susceptibility weighted imaging at very high field strength. *MAGMA* **21**:149-158. DOI: 10.1007/s10334-007-0101-3

Jensen JH, Lu H and Inglese M (2006) Microvessel density estimation in the human brain by means of dynamic contrast-enhanced echo-planar imaging. *Magn Reson Med* **56**:1145-1150. DOI: 10.1002/mrm.21052

Günther M (2006) Efficient visualization of vascular territories in the human brain by cycled arterial spin labeling MRI. *Magn Reson Med* **56**:671-675. DOI: 10.1002/mrm.20998

Liu C, Li W, Tong KA, Yeom KW and Kuzminski S (2015) Susceptibility-weighted imaging and quantitative susceptibility mapping in the brain. *J Magn Reson Imaging* **42**:23-41. DOI: 10.1002/jmri.24768

Mittal S, Wu Z, Neelavalli J and Haacke EM (2009) Susceptibility-weighted imaging: technical aspects and clinical applications, part 2. *AJNR Am J Neuroradiol* **30**:232-252. DOI: 10.3174/ajnr.A1461

Miyazaki M and Lee VS (2008) Nonenhanced MR Angiography. *Radiology* **248**:20-43. DOI: 10.1148/radiol.2481071497

Post JC, Van Rossum AC, Hofman MB, Valk J and Visser CA (1996) Three-dimensional respiratory-gated MR angiography of coronary arteries: comparison with conventional coronary angiography. *AJR Am J Roentgenol* **166**:1399-1404. DOI: 10.2214/ajr.166.6.8633453

Preim B and Oeltze S (2008) 3D visualization of vasculature: an overview. In: *Visualization in medicine and life sciences*. Springer Berlin Heidelberg, Germany, 39-59. DOI: 10.1007/978-3-540-72630-2_3

Reichenbach JR, Venkatesan R, Schillinger DJ, Kido DK and Haacke EM (1997) Small vessels in the human brain: MR venography with deoxyhemoglobin as an intrinsic contrast agent. *Radiology* **204**:272-277. DOI: 10.1148/radiology.204.1.9205259

Sakuma H (2011). Coronary CT versus MR angiography: the role of MR angiography. *Radiology* **258**:340-349. DOI: 10.1148/radiol.10100116

Sato Y, Nakajima S, Shiraga N, Atsumi H, Yoshida S, Koller T, Gerig G and Kikinis R (1998) Three-dimensional multi-scale line filter for segmentation and visualization of curvelinear structures in medical images. *Med Image Anal* **2**:143-168. DOI: 10.1016/S1361-8415(98)80009-1

Schuetz GM, Zacharopoulou NM, Schlattmann P and Dewey M (2010) Meta-analysis: noninvasive coronary

angiography using computed tomography versus magnetic resonance imaging. *Ann Intern Med* **152**:167-177. DOI: 10.7326/0003-4819-152-3-201002020-00008

Tropres I, Grimault S, Vaeth A, Grillon E, Julien C, Payen JF, Lamalle L and Decorps M (2001) Vessel size imaging. *Magn Reson Med* **45**:397-408. DOI: 10.1002/1522-2594(200103)45:3<397::AID-MRM1052>3.0.CO;2-3

Von Morze C, Xu D, Purcell DD, Hess CP, Mukherjee P, Saloner D, Kelley DA and Vigneron DB (2007) Intracranial time-of-flight MR angiography at 7T with comparison to 3T. *J Magn Reson Imaging* **26**:900-904. DOI: 10.1002/jmri.21097

Wang Y and Liu T (2015) Quantitative susceptibility mapping (QSM): decoding MRI data for a tissue magnetic biomarker. *Magn Reson Med* **73**:82-101. DOI: 10.1002/mrm.25358

Xiao C, Staring M, Wang Y, Shamonin DP and Stoel BC (2013) Multiscale bi-Gaussian filter for adjacent curvilinear structures detection with application to vasculature images. *IEEE Trans Image Process* **22**:174-188. DOI: 10.1109/TIP.2012.2216277